processes

MDPI

Article

Development of an FEM for the Combined Electromagnetic and Hydraulic Forming Process Based on Experimental Data

Yoonho Jang and Jeong Kim *

Department of Aerospace Engineering, Pusan National University, Busan 46241, Republic of Korea; rinnami430@pusan.ac.kr
* Correspondence: greatkj@pusan.ac.kr; Tel.: +82-51-510-2477

Abstract: Electrohydraulic forming (EHF) which demonstrates reduced bouncing effect, formation in narrow areas, and no effect on the electrical conductivity of the blank can overcome the shortcomings of deep drawing and electromagnetic forming. However, considerable time is involved in evaluating the possibility of forming a specific part through experiments. Developing an accurate finite element model can reduce the opportunity costs of an experiment by reducing unnecessary trial and error in forming a specific part. In this study, the chamber, die, and blank components of the EHF experimental equipment in our laboratory were reverse-modeled using CATIA V5R18. Subsequently, the IGES format of the components was imported into LS-DYNA R12, and an FEM model to simulate the EHF experiment was constructed. The experimental and simulation results of nine cases, based on the SUS430 material, input voltage, and blank thickness, were compared for model verification. The forming results for all cases in the constructed finite element analysis model nearly matched the experimental results. Moreover, the linear increase in the blank thickness with input voltage and thickness was simultaneously confirmed. In a computing environment using a 4.3 GHz, 24-Core CPU and 64 GB memory, the time required for one finite element analysis was approximately 1 h.

Keywords: high-speed forming; metal sheet forming; electrohydraulic forming (ehf); finite element analysis; experiment

Citation: Jang, Y.; Kim, J. Development of an FEM for the Combined Electromagnetic and Hydraulic Forming Process Based on Experimental Data. *Processes* **2024**, *12*, 2520. https://doi.org/10.3390/pr12112520

Academic Editor: Beatriz García-Baños

Received: 16 October 2024
Revised: 5 November 2024
Accepted: 11 November 2024
Published: 12 November 2024

1. Introduction

Metal sheet formation is an essential process in producing aircraft and automobile parts. The current trend toward lighter and stronger parts requires materials with higher strength per weight, such as high-strength steel and aluminum. However, the production costs involved in producing such parts cannot be ignored [1–3].

High-speed forming can compensate for the above-mentioned shortcomings and can replace drawing methods such as deep drawing, which uses a hydraulic press and die to form the specific features. High-speed forming includes electromagnetic forming, which uses the electromagnetic force generated by induced current, and explosive forming, which uses explosive materials to generate the forming force [4–7]. These references show that forming a highly conductive aluminum blank at high-speed using electromagnetic force enables deeper forming than that achieved with deep-drawing methods and that parts can be produced by explosive formation using TNT. High-speed forming can transform a blank into a shape suitable for a die by moving it at a high speed. When a rapidly accelerated blank collides with the die, a high strain rate occurs, and the stiffness of the material increases after forming [8,9]. These references show in their strain-stress diagrams that the yield and ultimate strength increase as the strain rate increases.

However, in electromagnetic and explosive forming, the forces that shape the metal blank are not applied through a medium with mass toward the die. Therefore, the duration of the forming force is short. This causes bouncing after the blank hits the die, and wrinkling occurs on the blank, degrading the product quality. In contrast, electrohydraulic forming

(EHF) uses a working fluid as a medium for the forming force, increasing the duration of the forming force [10]. Moreover, experiments using a free-bulging die showed that EHF produces wrinkle-free products. Figure 1 illustrates the EHF process. When a capacitor charged with high voltage is discharged rapidly, the current momentarily passes through the circuit connected by the wire between the two electrodes. The thin wire cannot endure the energy of the current and explodes. The explosive energy is transformed into kinetic energy in the working fluid inside the chamber and moves the blank toward the die, forming the blank.

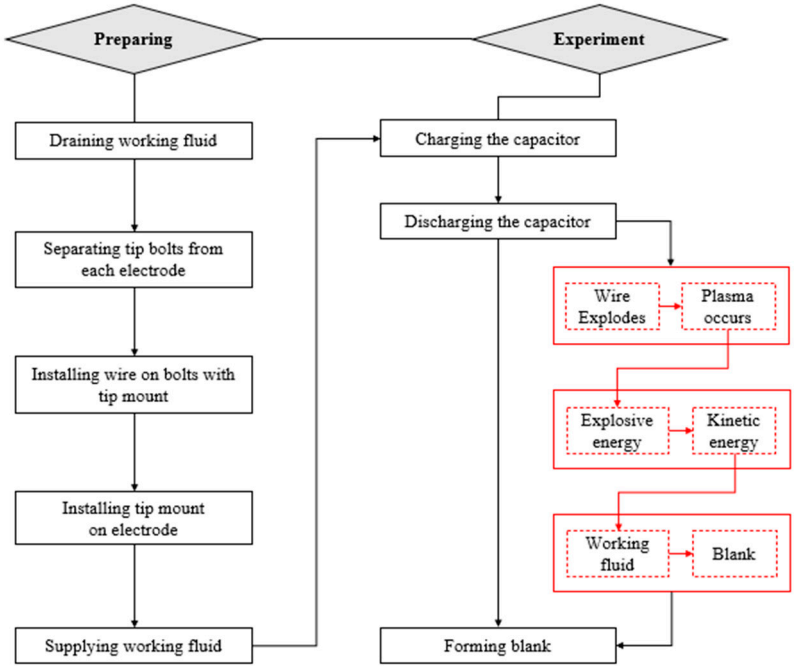

Figure 1. Process of EHF experiment.

EHF requires a working fluid supply and drainage process as well as the fastening of thin wires to drive the forming process. It is time-consuming compared to other high-speed forming methods. Accordingly, research has been conducted on finite element analysis models that seek to improve the time and cost efficiency of EHF processes [11,12]. The former research demonstrated methods of improving time and cost efficiency by modifying the EHF equipment to avoid using wires to reduce the EHF experiment time. The latter considered back-estimating the parameters to match the finite element analysis and experimental results for EHF experiments that do not match well.

However, in the former research, there is a disadvantage of lower energy efficiency, as the method used generates less forming energy than EHF using wires. In the latter research, by assuming a linear decrease in voltage and current over time and specifying the initial plasma size, a larger discrepancy of at least 10 mm arises before the results undergo the optimization process between the experimental results and the finite element analysis as the input voltage increases. In addition, research related to EHF finite element analysis models has covered the following issues.

The study "Finite Element Modelling of Electro-hydraulic Forming of Sheets", an EHF finite element analysis model was developed using the ABAQUS CAE 2022 software, where the input pulse was assumed as a reference rather than using energy data obtained from experimental results [13].

The study "Numerical modelling of electrohydraulic free-forming and die-forming of DP590 steel", similarly, used a calibrated acceleration value based on final dome height to set a baseline "energy multiplier factor" of 1.0, and represented the varying input energy level in the finite element analysis by adjusting the factor [14].

In the study "Experimental analysis and smoothed particle hydrodynamics modeling of electrohydraulic forming of sheet metal parts", finite element analyses of electrohydraulic forming were conducted using both the ALE and SPH methods. By comparing the results from these two methods, the study performed a comparative analysis between the simulation outcomes and the experimental results [15].

In this study, a finite element method (FEM) capable of simulating the same forming experiment as the EHF experimental equipment in the laboratory was constructed using CATIA V5R18 and LS-DYNA, and the experimental and numerical forming results were compared. For testing, three different sizes of SUS430 blanks, totaling nine samples, were used. Stainless steel, valued for its corrosion resistance, heat resistance, and durability, is crucial to the reliability and safety of aircraft and automobiles. High-speed forming produces stronger parts, allowing thinner automotive and aircraft components. Accordingly, the thicknesses of the blanks used in this study were set at 0.3 mm, 0.5 mm, and 0.7 mm, which include thinner values compared to the typical 0.5 mm to 1 mm thickness of aircraft sheets and automobile exterior panels [16]. Table 1 lists the material parameters for each experiment and the input voltages considered to confirm whether the FEM and experimental results are consistent.

Table 1. Electrohydraulic forming (EHF) test cases using blanks of SUS430 material.

Case	Specification of Blank			Input Voltage
	Thickness	Width	Length	
1-1	0.3 mm	250 mm	250 mm	6 kV
1-2				7 kV
1-3				8 kV
2-1	0.5 mm	230 mm	230 mm	6 kV
2-2				7 kV
2-3				8 kV
3-1	0.7 mm	230 mm	230 mm	6 kV
3-2				7 kV
3-3				8 kV

In contrast to conventional EHF finite element models, which assume linearly varying voltage and current data over time without a theoretical basis and directly model the origin of the initial forming force, this study set the initial volume of the forming force origin to almost zero based on mesh distribution. Thus, excessive forming force was avoided, which improved the comparisons to the experimental results. Furthermore, accurate time-dependent forming energy was used as an input parameter, resulting in finite element analysis outcomes closely matching the experimental results across various conditions.

The different SUS430 plastic properties were input according to the strain rate, and parts comprising a blank, die, and chamber that affected the forming process were used in the FEM [12]. Using the current and voltage over time data obtained using the Rogowski coil and probe, the forming force due to the wire explosion in the experiment was simulated. Moreover, the behavior of the fluid part and the contact between the solid and fluid features were simulated using a fluid–structure interaction based on the Arbitrary Lagrangian–Eulerian (ALE) method. Using a volume fraction technique that divides a single ALE part into multiple segments, the forming force (plasma) was modeled with an initial volume close to zero rather than direct boundary-conditioned modeling. This approach minimized the influence of mesh distribution, enabling the accurate finite element analysis of the contact conditions between Lagrange elements and thereby achieving precise finite element analysis results.

2. Experiment of EHF

2.1. Apparatus of EHF

Figures 2 and 3 show the 3D model of the EHF experimental equipment used in the laboratory and the assembly cross-section of the forming area, respectively. All of the unnecessary parts of the EHF equipment were excluded, and only the parts necessary for the FEM are shown in Figure 3. Under high-speed conditions, the shape of the sheet is influenced by the collision with the die. Hence, the die is completely open at the top for free bulging. The outer diameter, inner diameter, and radius of curvature are 150, 120, and 15 mm, respectively. The inside of the chamber is nozzle-shaped, and it has the same outer diameter as the die so that the behavior of the working fluid can be completely transmitted to the blank and die. The depth of the chamber is 100 mm. Two pairs of electrodes are inserted into the chamber and face each other at an angle of 20° from the ground. The electrodes are fixed to the outside of the chamber by a pulling screw to prevent the working fluid from leaking through the rubber packing. The pulling screw has a pitch of 2 mm per turn, allowing the electrode to move forward and backward.

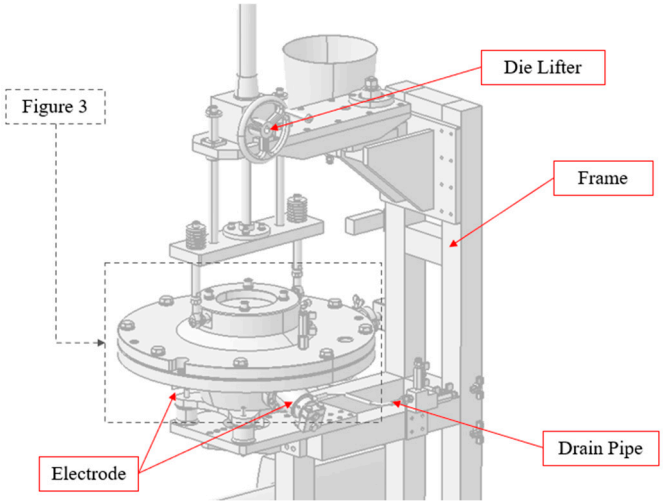

Figure 2. EHF apparatus: 3D model (Figure 3).

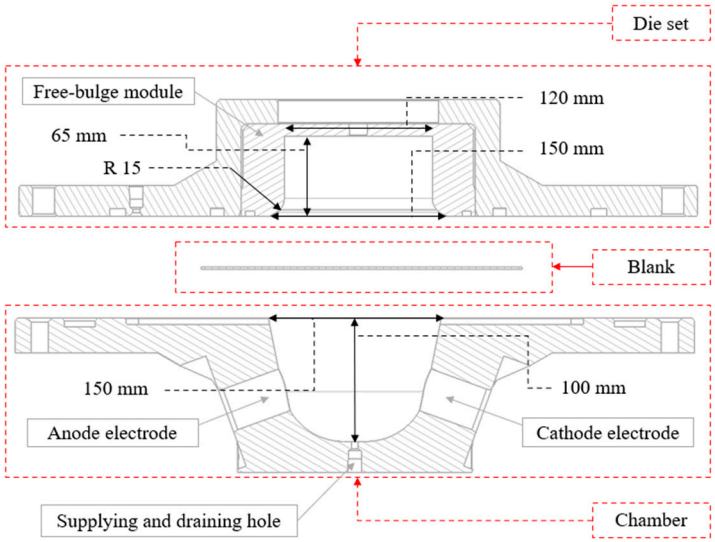

Figure 3. Cross-section of the essential parts of EHF.

An instantaneous high current through the electrode was delivered using a large capacitor in the laboratory. The specifications of the capacitor and experimental conditions under variable control are listed in Table 2.

Table 2. Specification of components for the EHF experiment.

Wire		Capacitor		Electrode	Working Fluid
Material	Diameter	Capacitance	Input Voltage	Material	Material
SUS304	0.1 mm	330 μF	6–8 kV	Al6061-T6	H_2O (liquid)

The distance between the two electrodes (electrode gap (EGAP)), representing the magnitude of the EHF force at the same input voltage and structure shape, and the distance between the blank and wire (called the standoff distance (SOD)) can be controlled. The EGAP and SOD are shown in Figure 4. Here, O and O_w are the center of the blank and fastened wire, respectively. According to the empirical results of the experimental equipment in our laboratory, the maximum forming force is generated when SOD = 35 mm and EGAP = 20 mm. Therefore, the forming experiments in this study maintained the above SOD and EGAP values.

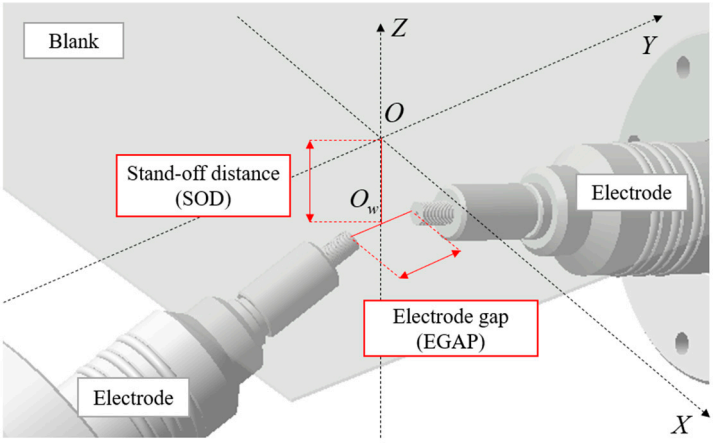

Figure 4. Locational parameters of EHF force.

2.2. Obtaining Experimental Voltage and Current

During the experiment, the voltage and current were measured using a probe and Rogowski coil, respectively. Because voltage and current are used as input variables to implement the forming force in the FEM described in Section 3, it is essential to validate the reliability of the FEM and experimental results. The magnitude of the electric energy between the electrodes can be obtained using the voltage and current data over time. The product of voltage and current at a specific point represents the instantaneous power at that specific time. Finally, the area of the power graph over time within the time of forming becomes the magnitude of the electric energy by definite integration, as shown in Equation (1). Here E_{total} is the total electric energy. T_0 and T_f are the start and end time of forming, respectively, and $i(t)$ and $V(t)$ are the time-dependent current and voltage measured using the Rogowski coil and probe, respectively. By theoretically obtaining the maximum energy that the capacitor can produce (Equation (2)) and comparing it with the measured electric energy, the electric efficiency of the EHF experimental equipment at each input voltage can be obtained. Here, E_c is the ideal electrical energy generated by a charged capacitor, C is the capacitance of the capacitor, and V_i is the input voltage before discharging the capacitor. Under ideal conditions, $E_{total} = E_c$, according to the law of conservation of energy. However, in reality, $E_{total} < E_c$ owing to energy consumption.

The specifications of the equipment used for current and voltage measurements are listed in Table 3.

$$E_{total} = \int_{T_0}^{T_f} i(t)V(t)dt, \tag{1}$$

$$E_C = \frac{1}{2}CV_i^2, \tag{2}$$

Table 3. Specifications of measuring instruments.

Oscilloscope	Rogowski Coil	Probe
TELEDYNE LECROY	CWT Rogowski	P6015A 1000X
HDO6054	Current Transducer	High Voltage Probe

The current graph, based on the input voltage measured under the conditions listed in Table 2, is shown in Figure 5. According to experiments, input voltages above 8 kV caused fractures in the 0.3 mm thick blank, while input voltages below 5 kV did not show significant forming results in the 0.7 mm thick blank. Therefore, this study utilized current and voltage data over time obtained from three input voltages: 6, 7, and 8 kV. The peak current is confirmed as 34.85 kA at 6 kV, 41.15 kA at 7 kV, and 48.05 kA at 8 kV. The current graph with respect to the input voltage when discharging the capacitor in the RLC circuit can be expressed using Equation (3), derived using Kirchhoff's voltage law and a second-order differential equation. Here, ω_0 is the resonant angular frequency, defined using Equation (4), and α is the Neper frequency, defined using Equation (5). For the EHF equipment in our laboratory, resistance R is 29 $m\Omega$, inductance L is 8 $\mu\Omega$, and capacitance C is 330 μF.

$$i(t) = \frac{V_i}{L\sqrt{\omega_0{}^2 - \alpha^2}} e^{-\alpha t} \sin\left(\sqrt{\omega_0{}^2 - \alpha^2 t}\right), \tag{3}$$

$$\omega_0 = \frac{1}{\sqrt{LC}}, \tag{4}$$

$$\alpha = \frac{R}{2L}, \tag{5}$$

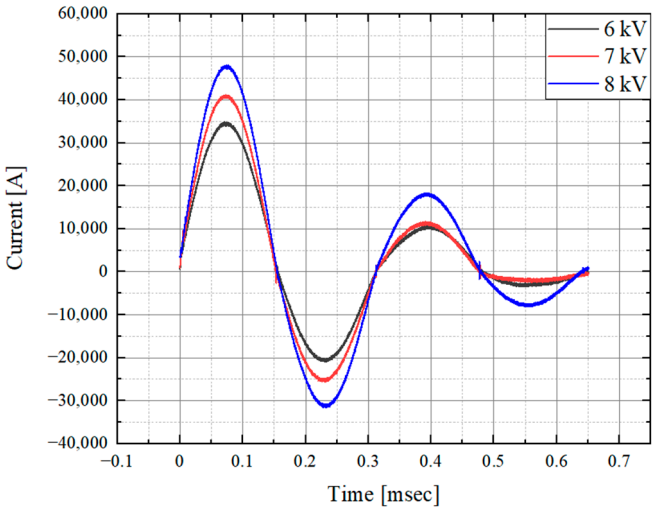

Figure 5. Current curves measured by Rogowski coil and oscilloscope.

In the case of a fully closed circuit, the voltage over time given by Equation (6), measured by the sudden discharge of the capacitor, can be defined using Equation (3) [17]. However, in the case of the EHF equipment circuit, as soon as the capacitor is discharged,

the wire explodes, forming an open circuit. Despite the open circuit, current exists. Therefore, an unusual voltage graph is measured, where the voltage does not become zero at the point where the measured AC is maximum.

The graphs of the voltage over time measured in the circuit, where the discharged capacitor is connected according to each input voltage, are shown in Figure 6. Compared to the theoretical equation, the initial voltage should be the same as the voltage to charge the capacitor. However, it shows a reduction of more than four times. The voltages measured when the capacitor is discharged at input voltages of 6, 7, and 8 kV are 1.957, 1.872, and 1.783 kV, respectively. Although the current data shows a clear difference over time depending on the input voltage, there is no significant difference in the magnitude of the voltage over time depending on the input voltage [18]. In other words, the shaping force of EHF during capacitor discharging is dominated by current. The power graph, calculated by multiplying the current and voltage measured at each input voltage, is shown in Figure 7. The electric energy graph is shown in Figure 8.

$$V(t) = V_i - \left[\frac{1}{C}\int_{T_0}^{T_f} -i(t)d(t)\right], \tag{6}$$

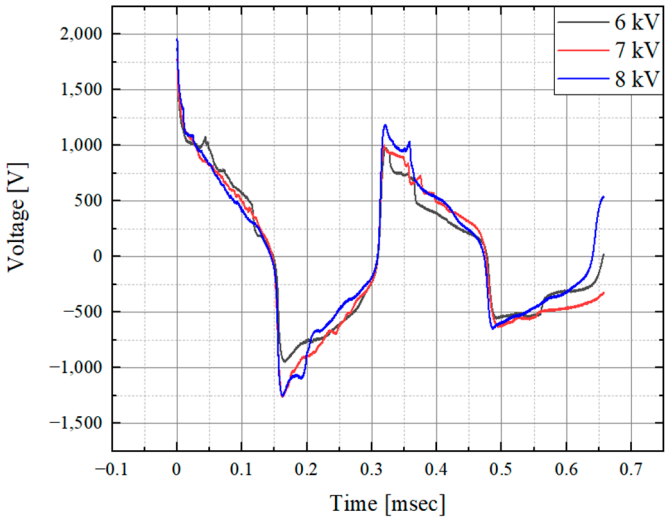

Figure 6. Voltage curves measured by probe and oscilloscope.

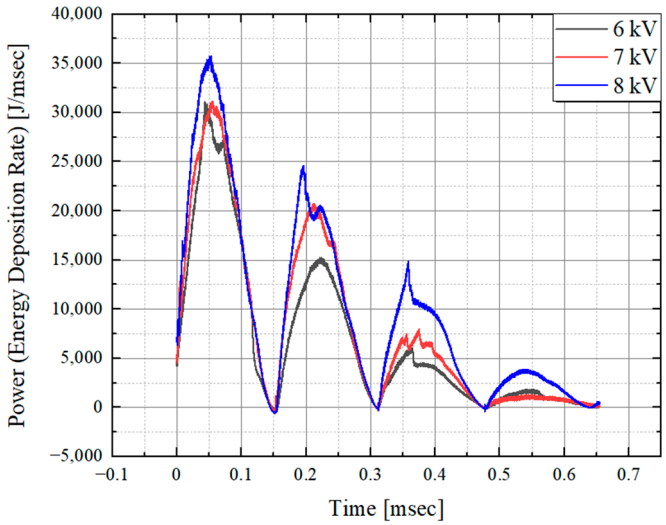

Figure 7. Power curve calculated by the measured voltage and current.

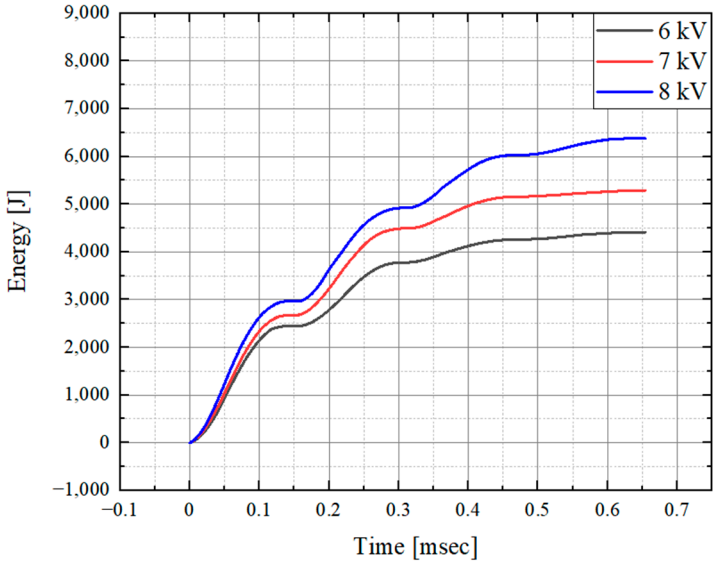

Figure 8. Electric energy curve calculated by integrating the power curve.

2.3. Experimental Results

Experiments were conducted for the nine cases presented in Table 1. After the experiments' completion, the blanks were 3D scanned to determine the point where the maximum bulge height was measured. As shown in Figure 9, the plane passing through the two points where the wires are connected to each electrode and the center of the upper part of the chamber is captured and moved parallel to the point corresponding to the maximum bulge height. Subsequently, the formed blank is projected. Thus, a 2D contour is obtained for each formed blank. The EHF experimental results for SUS430 blanks with a thickness of 0.3 mm at input voltages of 6, 7, and 8 kV are shown in Figure 10. Similarly, the results for blank thicknesses of 0.5 and 0.7 mm are shown in Figures 11 and 12, respectively.

Following the results, the x coordinate of the peak point is not constant due to the experimental conditions. As a free-bulging die is used, it shows non-symmetrical shapes when the position of the forming force is slightly off. Matching the peak point is not easy, as the process of connecting the wire to concentrate the force on the center of the chamber is delicate work. This proves that an FEM model for EHF, which involves a difficult experimental process, is absolutely necessary. The Z coordinate of the peak point increases linearly as the input voltage increases. This shows that the thicker the blank, the easier it is to create symmetrical results. It takes several experiments for each case to create those figures. In Figures 10 and 11, the points where the z coordinate is negative are the points at which the blank was partially sucked into the working fluid draining zone on the chamber.

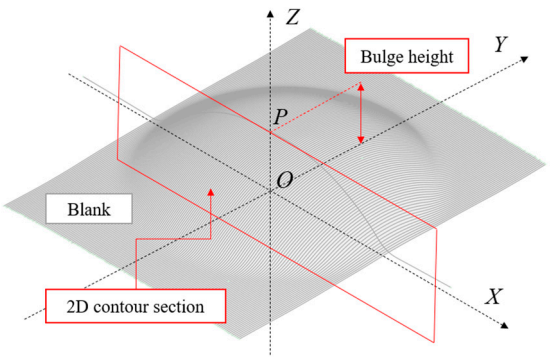

Figure 9. Schematic of surface measurement obtained for 2D contour.

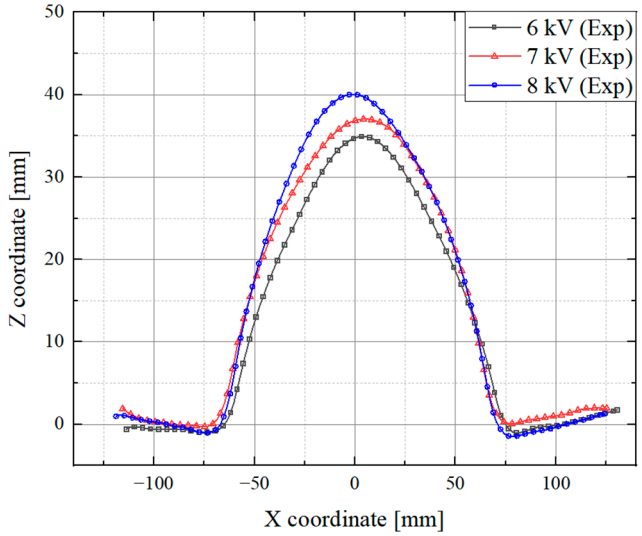

Figure 10. Experimental result of 0.3 mm blank.

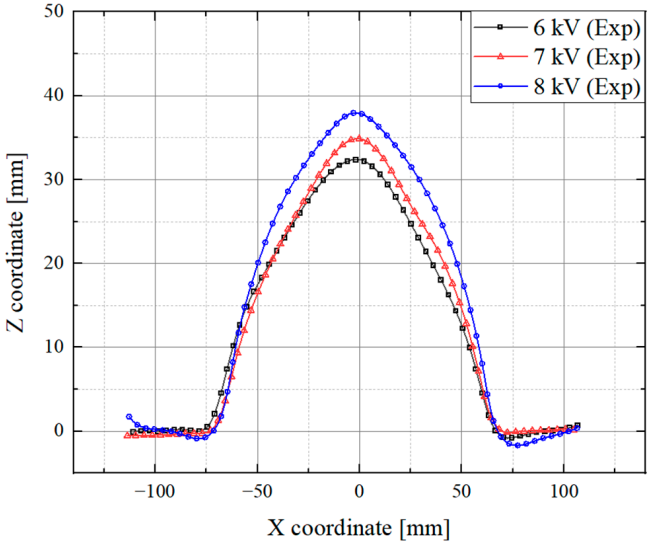

Figure 11. Experimental result of 0.5 mm blank.

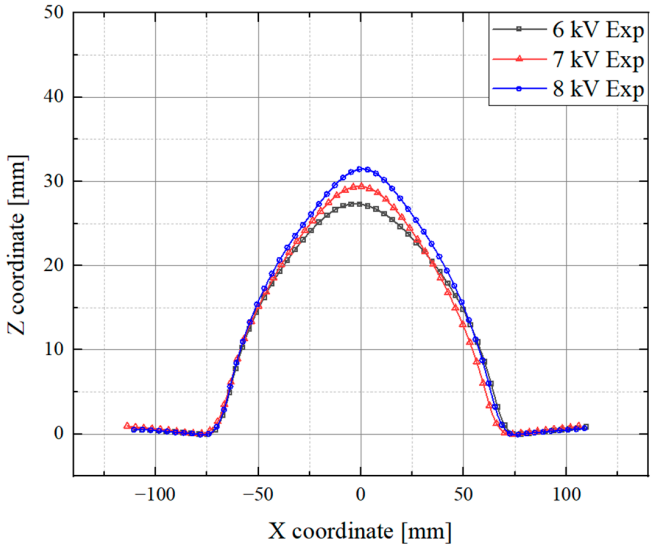

Figure 12. Experimental result of 0.7 mm blank.

3. Finite Element Model of EHF

3.1. Geometry Creation for FEM

The dimensions and scale of the die and chamber from the experimental equipment were replicated utilizing the 3D model of the EHF equipment in our laboratory, which was constructed using shell elements. We modeled the structural parts, namely the die, blank, and chamber for the FEM, using shell elements by offsetting the surface. Parts not necessary for analysis, such as electrodes, wires, and drain holes, were excluded from the FEM model to facilitate the analysis.

Parts of the working fluid and surrounding air were modeled separately as solid elements. Because the surrounding air only needs to be created in an area that can include the inside of the chamber and die, only the area where the working fluid can flow was modeled in the form of a rectangle to reduce the computing time of the FEM. The working fluid was modeled as being completely contained inside the chamber. This part does not directly play the role of the working fluid and is used as the boundary between the surrounding air and working fluid. Figure 13 shows the modeling of the solid and shell models created for FEM. The sizes of all of the parts are identical to those of the experimental equipment in Figure 3.

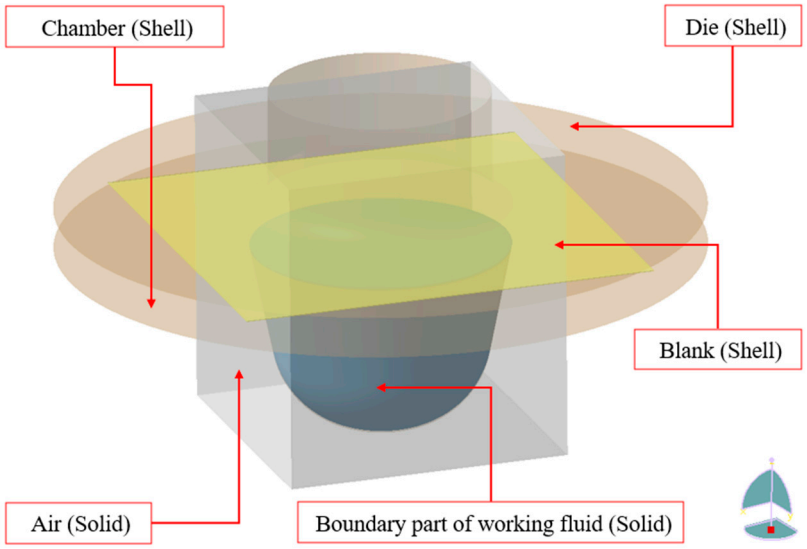

Figure 13. Modeling of the EHF components for finite element method (FEM).

Following the creation of the model, ABAQUS CAE 2022 software was utilized to mesh 1/4 of the area surrounding the center of the chamber and die. Each part was then symmetrically moved to complete the geometry of the complete FEM, comprising the elements and nodes. The structural part comprised S4 (4-node) shell elements, while the fluid part comprised C3D8 (3D 8-node linear iso-parametric element) solid elements.

The mesh size was adjusted to be as similar as possible to implement the fluid–structure interaction. The mesh sizes of the fluid and structural parts were configured to approximately 1.75–2 mm by subdividing the partitions of the structural parts. The parts finally created for the FEM are the five structural parts: die, chamber, blank and fluid part, working fluid, and surrounding air. In addition, during finite element analysis, the air part is divided into three Arbitrary Lagrangian–Eulerian parts: the surrounding air, working fluid, and plasma as the energy-generating element, as described in Section 3.3.

The plasma was assumed to be spherical and was set to expand at the start of the simulation with zero volume. The location of the plasma was set to be 35 mm lower than that of the blank at the center of the chamber, the same as the SOD of the experimental conditions. Part of the working fluid modeled as a solid element was set to contain the keyword necessary to generate the working fluid along the boundary. Through this process, the initial working fluid was simulated to be completely filled inside the chamber,

confirming plasma generation inside the working fluid. The surrounding air was divided into three parts, as shown in Figure 14, which is a quarter section of the FEM model.

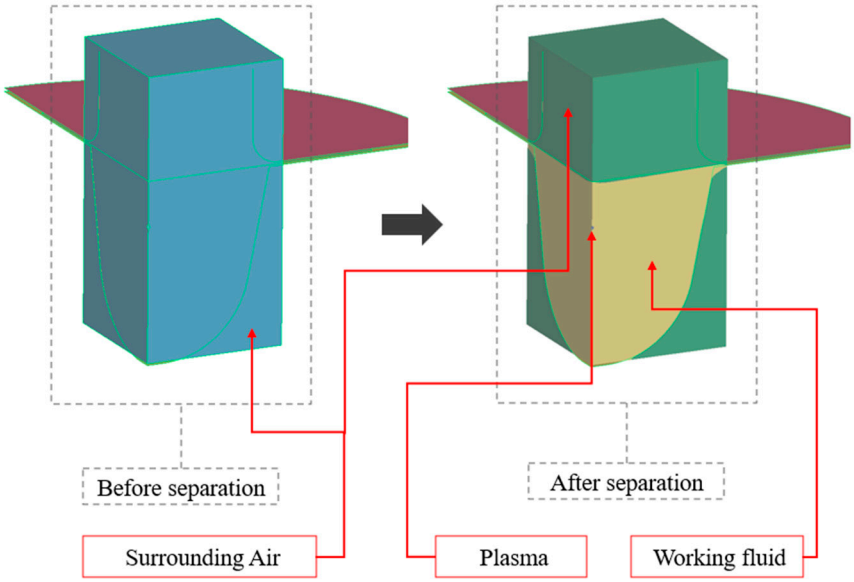

Figure 14. Arbitrary Lagrangian–Eulerian part divided into plasma, working fluid, and surrounding air.

3.2. Material Properties for FEM

First, the material properties were input into the structural parts comprising a die, blank, and chamber that make up each geometry. The die and chamber were assumed to be rigid bodies without deformation. Accordingly, the material properties of the elastic range of SNCM439, which are the same as those of the material that constitutes the actual die and chamber, were input. The elastic material properties of SNCM439 are shown in Table 4 and were input using the 'MAT_020_RIGID' keyword in LS-DYNA [19]. The shell thicknesses of the die and chamber were set to 1 mm.

Table 4. Elastic material properties of SNCM439.

Density [kg/m^3]	Young's Modulus [GPa]	Poisson's Ratio	Yield Strength [GPa]
7850	196	0.33	1.550

For the blank, the SUS430 material properties, considering the strain rate, were input. The material properties were obtained by inverse-estimating the coefficients of the Cowper–Symonds constitutive equation and are material within the strain rate range of 1/s to 10,000/s [12]. The strain-stress curve according to strain rate using the 'DEFINE_CURVE' keyword of LS-DYNA was combined with the 'DEFINE_TABLE' keyword and input into the 'MAT_024_PIECEWISE_PLASTICITY' keyword to simulate the elastic and plastic behaviors of an isotropic material. The thicknesses of the blanks in the shell elements were specified as 0.3 mm, 0.5, and 0.7 mm, the same as in the experiments. The elastic properties of SUS430 are shown in Table 5, and the plastic region strain-stress curves obtained at strain rates of 1, 10, 100, 1000, 10,000/s are shown in Figure 15.

Table 5. Elastic material properties of SUS430.

Density [kg/m^3]	Young's Modulus [GPa]	Poisson's Ratio	Yield Strength [GPa]
7800	200	0.33	0.274

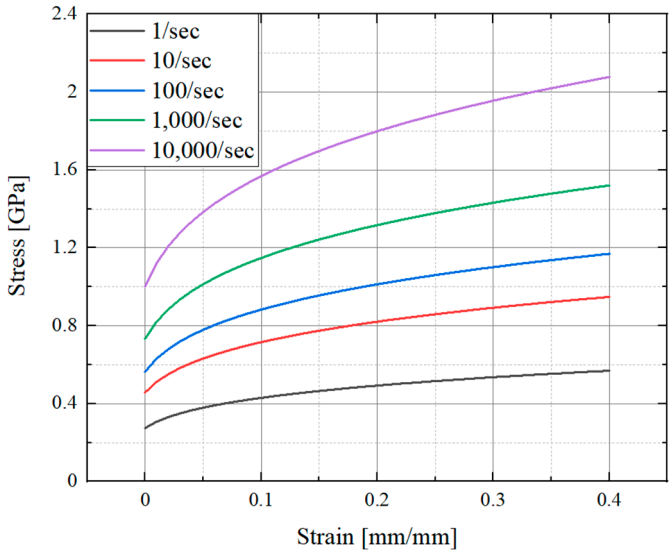

Figure 15. Plastic region strain-stress diagram of SUS430 according to the strain rate.

The fluid parts simulated the behavior of the working fluid, air, and plasma in this FEM using the ALE method.

For the working fluid, the keyword 'MAT_001_ELASTIC_FLUID' was used to input the material properties based on bulk modulus and density. In this study, the water used for EHF in the laboratory was set as the working fluid. The properties applied to the keywords are listed in Table 6.

Table 6. Material properties of the working fluid.

Material	Bulk Modulus [GPa]	Density [kg/m^3]
Water (H_2O)	2.345	1000

For the surrounding air and plasma, the keyword in LS-DYNA 'EOS_LINEAR_ POLYNOMIAL_WITH_ENERGY_LEAK' based on the equation of status was used. The keywords were simulated based on Equation (7), defined as a linear polynomial equation of the pressure and internal energy. Here, P is the pressure, C is the coefficient of each term, μ is the ratio of the initial density to the density at a specific time, and E is the internal energy per unit reference volume.

For the EHF experiment, this study assumed that the energy owing to the generation and expansion of the plasma after the wire explosion is transferred to the air around the plasma, because the plasma is in an ionized state and has almost no mass. Therefore, the properties of the plasma and surrounding air were assumed to be identical to those of an ideal gas. According to the LS-DYNA manual, in the case of an ideal gas, the coefficients of Equation (7) are defined as in Equations (8) and (9). Here, γ is the ratio of the specific heat, C_p is the specific heat at a constant pressure, and C_v is the specific heat at a constant volume. The properties of the surrounding air and plasma are listed in Table 7. Subsequently, the power to create the forming force was applied to the plasma. The 'EOS_LINEAR_POLYNOMIAL_WITH_ENERGY_LEAK' keyword can simulate the forming force to a specific part by receiving the energy deposition rate, which is proportional to the electric power, the energy transferred per unit time, as input. The raw electric power data obtained in Section 2.2 was incorporated using the 'DEFINE_CURVE' keyword and applied to the aforementioned keyword.

$$P = C_0 + C_1\mu + C_2\mu^2 + C_3\mu^3 + \left(C_4 + C_5\mu + C_6\mu^2\right)E, \quad (7)$$

$$C_0 = C_1 = C_2 = C_3 = C_6 = 0, \quad (8)$$

$$C_4 = C_5 = \gamma - 1 = \frac{C_p}{C_v} - 1 = 0.4. \quad (9)$$

3.3. Boundary Condition of FEM

The contact condition of the structural part used LS-DYNA's 'CONTACT_SURFACE_TO_SURFACE' keyword. As the die and chamber do not come into direct contact, contact conditions were applied to the contact surfaces of the die and blank as well as the blank and chamber. All structural parts are in contact with the shell shapes. Therefore, the 'SHLTHK' parameter was set to '2' in the 'CONTROL_CONTACT' keyword to incorporate thickness considerations. The die was treated as a rigid body, while the chamber and blank were treated as deformable bodies with sufficient thickness, preventing wrinkling during forming.

During the fluid–structure interaction, the keyword CONSTRAINED_LAGRANGE_IN_SOLID simulates the contact between the ALE and structural parts. However, when simulating a case in which a contact between the structural and ALE parts occurs at a high speed, such as EHF, it is difficult to provide the contact conditions because of the high penetration possibility. Therefore, the input parameters of the penalty factor, coupling leakage control flag, leakage control penalty factor, and minimum volume fraction to activate coupling should be appropriately controlled to simulate the contact conditions. The values used in this study are given in Table 7.

Table 7. Input parameters for the CONSTRAINED_LAGRANGE_IN_SOLID keyword.

PFAC	ILEAK	PLEAK	FRCMIN
0.2	2	0.1	0.5

The forming force, plasma, was configured as a spherical shape with a 0.01 mm radius, positioned 35 mm from the blank along the chamber's central axis at the start of the finite element analysis. Previously, to achieve accurate results, the minimum possible radius was at least 2 mm, requiring adjustments to the surrounding working fluid and direct modeling of this part. However, with automatic ALE element generation during finite element analysis, the part size could be significantly reduced without additional artificial adjustments.

The initially generated plasma part expands according to the power curve over time, which was experimentally obtained based on the discharge voltage in Section 2.2. Using the ALE_MULTI-MATERIAL_GROUP keyword, boundary conditions were set to ensure that the plasma remained separate from the working fluid, allowing all of the energy to be fully transmitted to the working fluid.

To impose the same conditions as in the experiment, the chamber and die were constrained for translational motion in the X, Y, and Z directions and rotational motion in the XY, YZ, and ZX directions. No constraints were imposed on the behavior of the blank and ALE parts. The position of the chamber was fixed according to the thickness of the blank, which varied so that the blank could be completely fixed between the chamber and die. Furthermore, the z-direction height of the die and blank was changed so that the three structural parts were completely attached without a gap so that the simulation could be performed in the desired manner. Finally, finite element analyses were conducted for the nine cases. A representative model of the simulation process is shown in Figure 16.

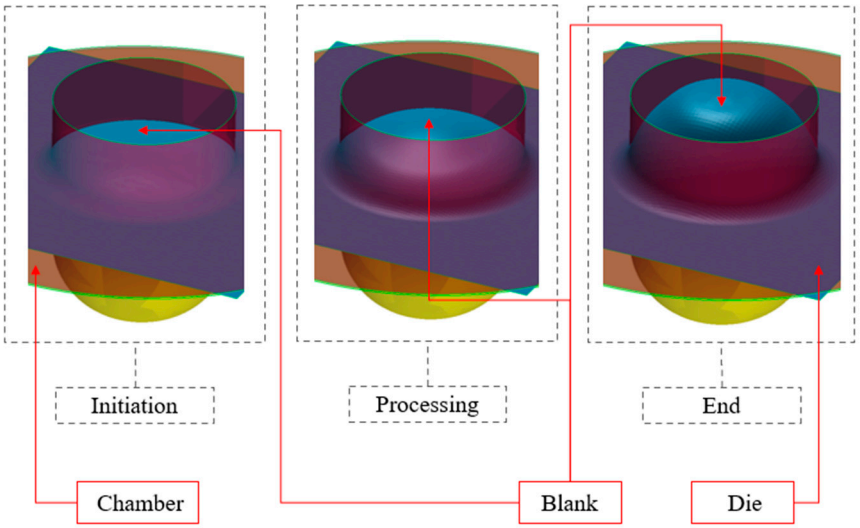

Figure 16. Simulation process of constructed EHF FEM.

3.4. Results of FEM

Simulations were conducted for the nine cases presented in Table 1. In each simulation, the maximum bulge height was measured, and the 2D contours of each FEM were obtained based on the point passing through the maximum bulge height, similar to the EHF experiment described in Section 2.

The specifications of the computer used in this FEM are as follows: AMD RYZEN THREADRIPPER 3960X CPU with 24 cores and 48 threads with 4.3 GHz, 64 GB of memory. The time required for a complete analysis was approximately 1 h under a 0.005 ms timestep and 1 ms termination time. The version of LS-Prepost used to build the FEM was 2024/R2(4.11.6), and the LS-Dyna solver used was ls-dyna_smp_s_R12_149128_winx64

Only blank shapes for which the EHF simulation was conducted under each experimental condition are presented. The FEM results of the SUS430 blanks with a thickness of 0.3, 0.5, and 0.7 mm are shown in Figure 17, Figure 18, and Figure 19, respectively, at input voltages of 6, 7, and 8 kV. The FEM results show that, unlike the complex process experiments and results, a symmetrical shape can be created with almost the same peak points as those found in the experiments.

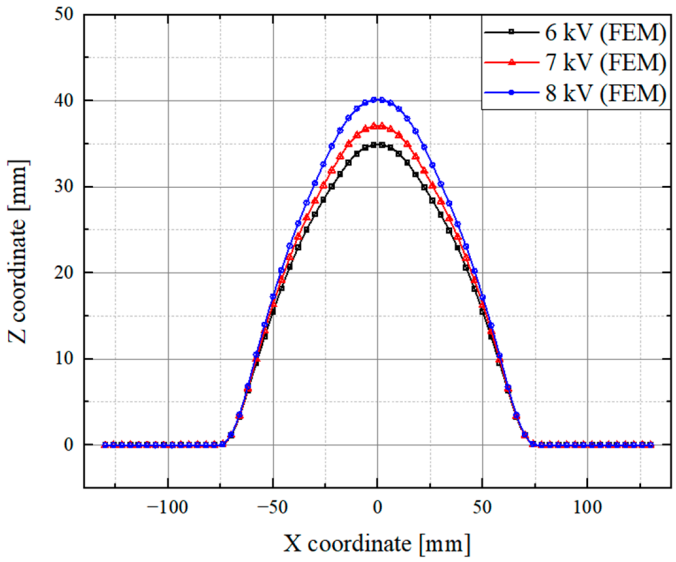

Figure 17. Simulation result with 0.3 mm blank.

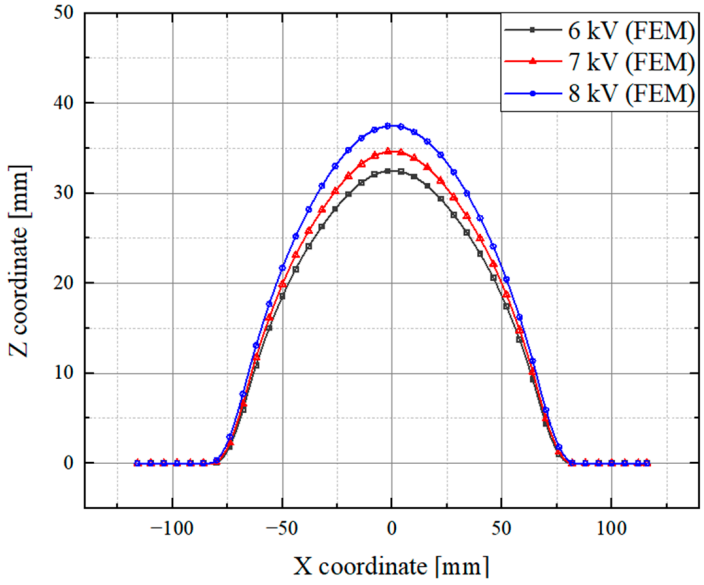

Figure 18. Simulation result with 0.5 mm blank.

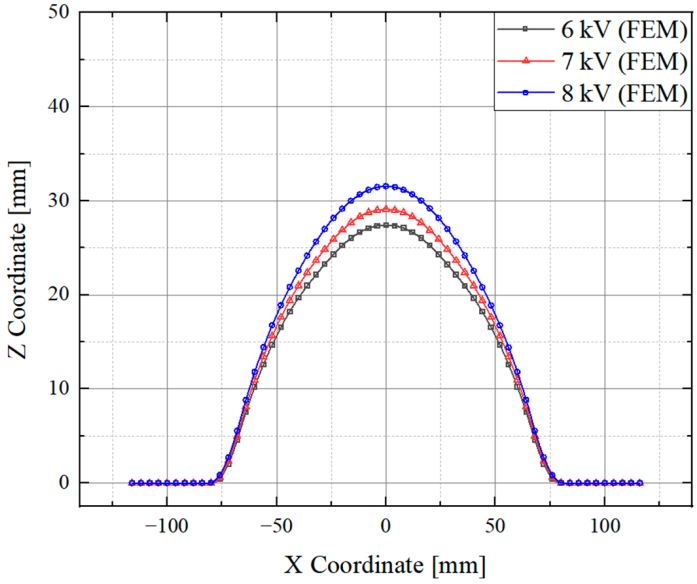

Figure 19. Simulation result with 0.7 mm blank.

4. Conclusions

The 2D contours of the experimental and FEM results obtained at blank thicknesses of 0.3, 0.5, and 0.7 mm are compared in Figure 20, Figure 21, and Figure 22, respectively. The maximum bulge height error between the experimental and FEM results in each case, as listed in Table 8, is within 0.46 mm at Figure 21c, which is acceptable. This error may have occurred because of the capacitor characteristics. The minimum measurement unit of the charging voltage gauge of the capacitor in the laboratory is 0.1 kV, indicating a voltage between $\alpha-$ 0.1 kV and $\alpha+$ 0.1 kV for α kV input voltage.

The comparative analysis of the experimental and FEM results at various voltage conditions confirms that the maximum bulge height and forming distribution in the area surrounding the peak point are almost the same. This indicates that the radial energy distribution generated closely mirrors the experimental energy and forming force direction at each input voltage, as observed in the EHF experiment.

Figures 20, 21 and 22a–c display the finite element analysis and EHF experiment results for each input voltage. Each figure shows slight differences in forming height around the

maximum bulge measurement area, with no specific trend of increase or decrease with rising input voltage. In Figure 20, the largest forming height difference around the periphery appears at 7 kV (Figure 20b), while the smallest is at 6 kV (Figure 20a). In Figure 21, the 7 kV condition in Figure 21b shows the greatest difference, and 8 kV in Figure 21c shows the smallest. In Figure 22, the maximum height difference is at 8 kV (Figure 22c), and the minimum is at 6 kV (Figure 22a).

The height difference arises from SOD variations during the wire setup in the EHF experiments. In the finite element model, the explosion point of the wire is fixed as a boundary condition, maintaining a constant direction of spherical forming force on the blank across input voltages. Thus, a consistent peripheral forming distribution is achieved regardless of voltage, as shown in Figures 17–19. In the experiments, however, slight SOD deviations occur due to the difficulty of uniformly tensioning the wire, leading to differences in the peripheral forming height between the finite element analysis and the experimental results. A larger SOD reduces the horizontal forming force due to increased blank and die distance, while a smaller SOD increases it due to closer proximity [20]. Paradoxically, a well-constructed finite element model can save considerable time and material cost by eliminating the need for extensive experimental trials while still replicating experimental results accurately.

In a finite element analysis of very thin blanks, results often show greater deviations from experimental outcomes than analyses performed using thicker blanks [21]. However, this finite element analysis model demonstrates minimal discrepancies between experimental and simulation results even for thin blanks by adjusting only the blank thickness and experimentally measured forming energy. This improvement is attributed to the carefully calibrated input parameters used in the finite element model, as outlined in Table 7, which successfully mitigates the typical challenges associated with simulating thin blank forming.

Figure 23 shows the maximum bulge height of each experiment and FEM. The experimental and FEM results are in almost perfectly matched. For blanks of the same thickness, the maximum bulge height was found to increase almost linearly with increasing input voltage in both experimental and FEM results.

When comparing the differences between the experimental and finite element analysis results at the same voltage for blanks of 0.5 mm and 0.3 mm thickness with those for blanks of 0.7 mm and 0.5 mm thickness (see Figure 23), we observed that the rate of increase of the forming height decreased when using a 0.3 mm thick blank. As indicated in Table 1 of Section 1, the 0.3 mm blank has a greater width and length than blanks of the other thicknesses, resulting in a stronger blank holder force [22]. The agreement between the experimental and finite element analysis results confirms that the finite element model accurately accounts for the varying blank holder force.

Table 8. Comparing maximum free-bulge height from the experiment and FEM results (Unit: mm).

Voltage		**6 kV**			**7 kV**			**8 kV**	
Thickness	**Exp**	**FEM**	**Error**	**Exp**	**FEM**	**Error**	**Exp**	**FEM**	**Error**
0.3 mm	34.91	34.94	0.03	37.04	37.09	0.05	40.04	40.17	0.13
0.5 mm	32.39	32.51	0.12	34.88	34.68	0.20	37.96	37.50	0.46
0.7 mm	27.33	27.43	0.10	29.41	29.09	0.32	31.48	31.56	0.08

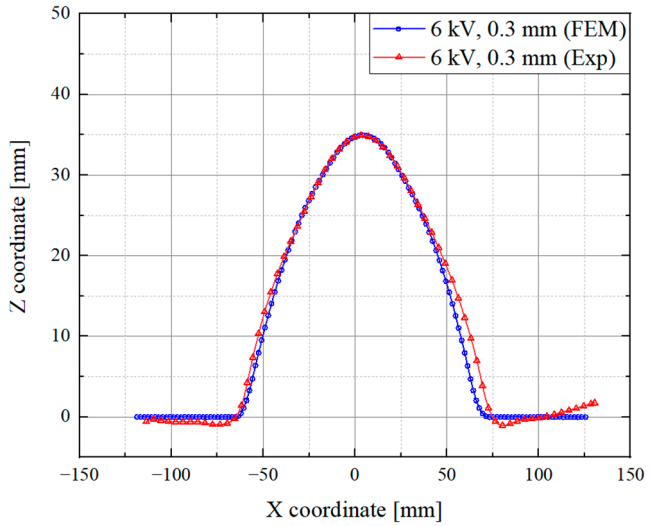

(**a**)

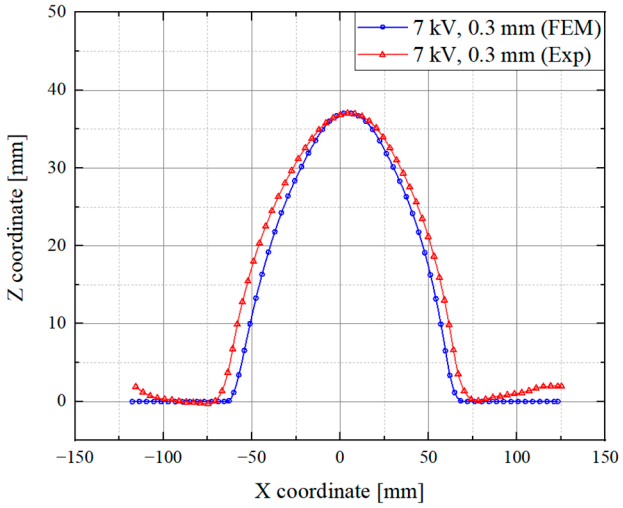

(**b**)

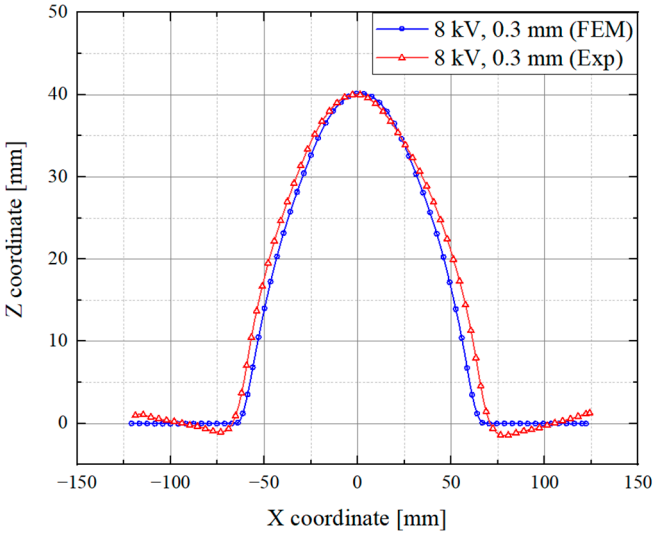

(**c**)

Figure 20. (**a**) Simulation and experimental results with 0.3 mm blank and 6 kV input voltage. (**b**) Simulation and experimental results with 0.3 mm blank and 7 kV input voltage. (**c**) Simulation and experimental results with 0.3 mm blank and 8 kV input voltage.

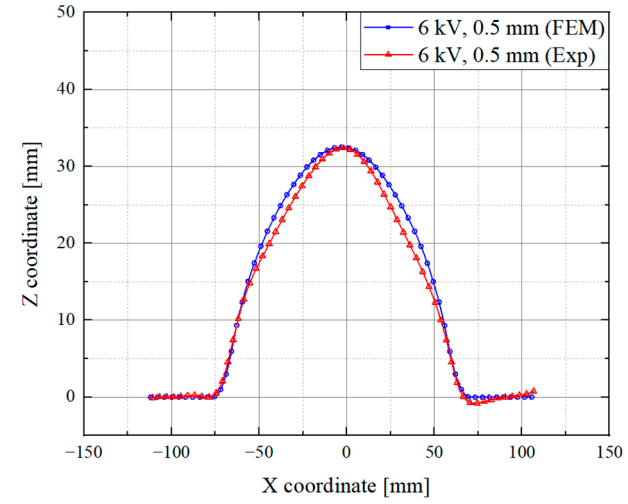

(**a**)

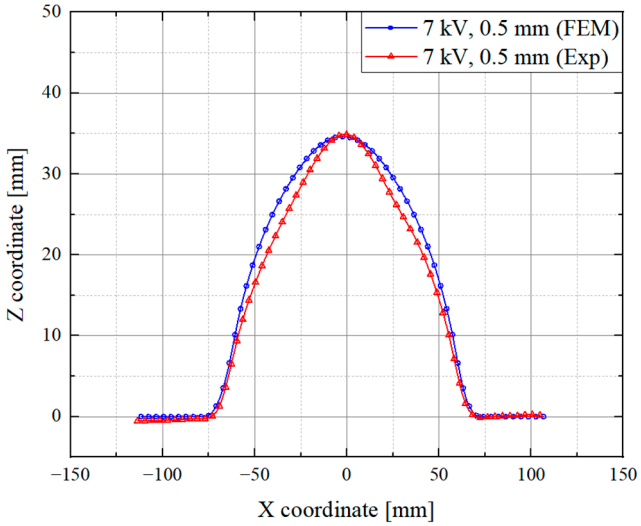

(**b**)

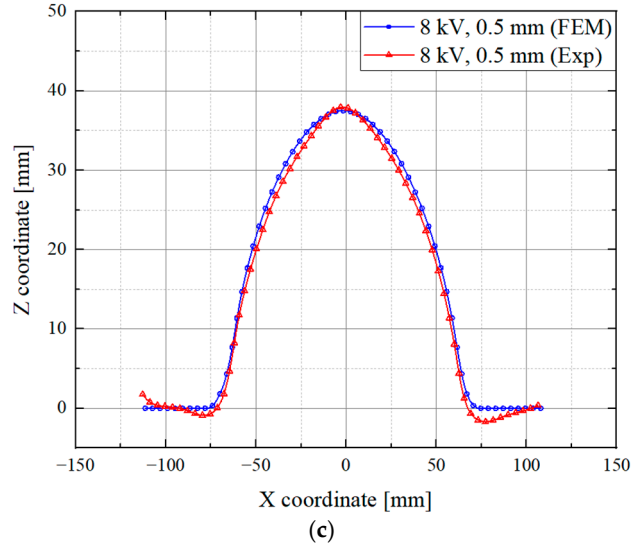

(**c**)

Figure 21. (**a**) Simulation and experimental results with 0.5 mm blank and 6 kV input voltage. (**b**) Simulation and experimental results with 0.5 mm blank and 7 kV input voltage. (**c**) Simulation and experimental results with 0.5 mm blank and 8 kV input voltage.

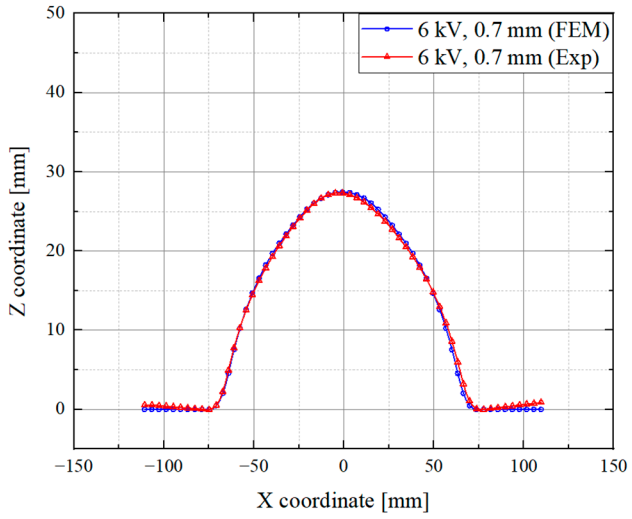

(**a**)

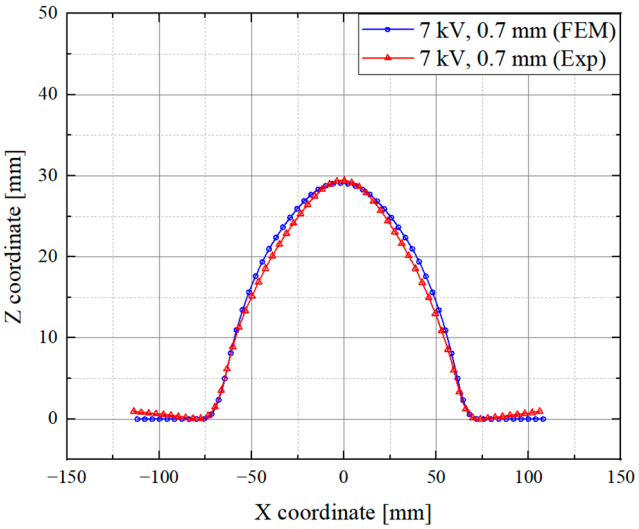

(**b**)

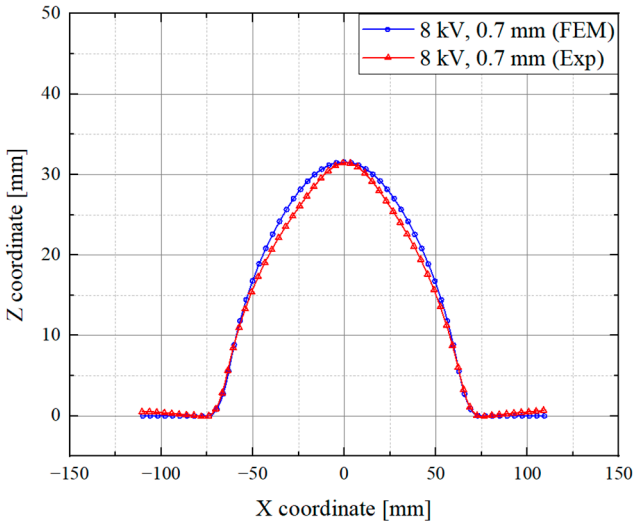

(**c**)

Figure 22. (**a**) Simulation and experimental results with 0.7 mm blank and 6 kV input voltage. (**b**) Simulation and experimental results with 0.7 mm blank and 7 kV input voltage. (**c**) Simulation and experimental results with 0.7 mm blank and 8 kV input voltage.

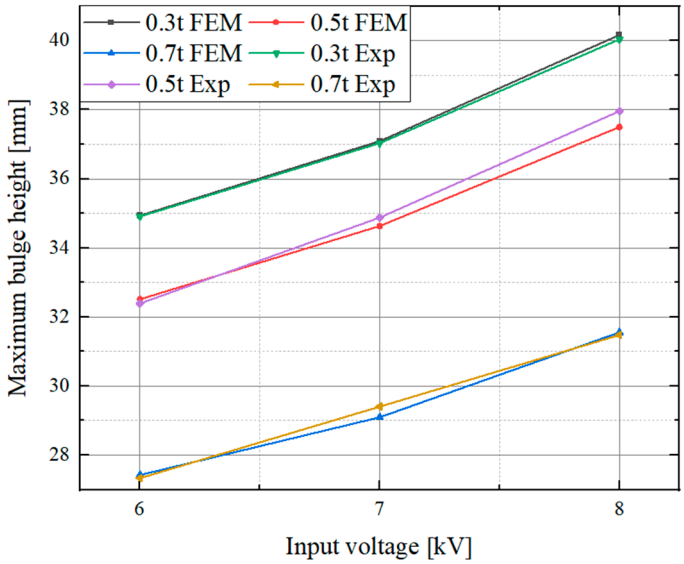

Figure 23. Increase rate of the maximum bulge height with input voltage for each specimen.

This study constructed an FEM model capable of simulating an EHF experiment by comparing several experimental results. The main findings are as follows:

1. To define the input parameters of the finite element model, voltage and current measurements were conducted for three different input voltages, and the experiments were simulated using fluid–structure interaction analysis. Previous studies did not accurately measure voltage and current data over time, leading to imprecise input parameters that prevented achieving finite element analysis results consistent with experimental outcomes.
2. In the finite element analysis program, the elastic properties of the SUS430 material, plastic properties based on the Cowper–Symonds constitutive equation, and boundary condition parameters were kept constant. By modifying the electrical energy according to the measured input voltage and the thickness of the blanks only, the maximum forming heights obtained from both the experimental and FEM results were nearly identical.
3. The finite element model developed in this study provides a more reliable forming distribution around the maximum bulge height point compared to results from the laboratory EHF experimental setup. This highlights the model's advantage, as it allows for quick and easy validation without complex experimental procedures. The limitation in the laboratory apparatus arises from the need to manually fasten the wire, making it challenging to control experimental variables like SOD effectively.

Author Contributions: Exploring conception and design for experiment, material preparation, experiment, construction of finite element model and analysis and data collection were performed by Y.J. The first draft of the manuscript was written by Y.J. and J.K. commented on previous versions of the manuscript. All authors have read and agreed to the published version of the manuscript.

Funding: This research was supported by a National Research Foundation of Korea (NRF) grant funded by the Korean government (MSIT) through the Ministry of Science and Technology (RS-2023-00253461621820653000001). This research was also supported by the BK21 FOUR (Fostering Outstanding Universities for Research) funded by the Ministry of Education (MOE, Korea) (5199990714554).

Data Availability Statement: The data presented in this study are available on request to the corresponding author.

Conflicts of Interest: The funders had no role in the design of the study. The authors declare no potential conflicts of interest.

References

1. Atzeni, E.; Iuliano, L.; Marchnindi, G.; Minetola; Salmi, A. Additive manufacturing as a cost-effective way to produce metal parts. In Proceedings of the Advanced Research and Rapid Prototyping, Leiria, Portugal, 1–5 October 2013; pp. 3–8.
2. Costabile, G.; Fera, M.; Fruggiero, F.; Lambiase, A.; Pham, D. Cost models of additive manufacturing: A literature review. *Eng. Mater. Scinece* **2016**, *8*, 263–283. [CrossRef]
3. Anzalone, G.C.; Zhang, C.; Wijnen, B.; Sanders, P.G.; Pearce, J.M. A Low-Cost Open-Source Metal 3-D Printer. *IEEE Access* **2013**, *1*, 803–810. [CrossRef]
4. Gayakwad, D.; Dargar, M.K.; Sharma, P.K.; Prohit, R.; Rana, R.S. A review on Electromagnetic Forming Process. *Procedia Mater. Sci.* **2014**, *6*, 520–527. [CrossRef]
5. Mamalis, A.G.; Manolakos, D.E.; Kladas, A.G.; Koumoutsos, A.K. Electromagnetic Forming Tools and Processing Conditions: Numerical Simulation. *Mater. Manuf. Process.* **2006**, *21*, 411–423. [CrossRef]
6. Lai, Z.; Cao, Q.; Han, X.; Liu, N.; Li, X.; Huang, Y.; Chen, M.; Cai, H.; Wang, G.; Liu, L.; et al. A comprehensive electromagnetic forming approach for large sheet metal forming. *Procedia Eng.* **2017**, *207*, 54–59. [CrossRef]
7. Akbari Mousavi, S.A.A.; Riahi, M.; Hagh Parast, A. Experimental and numerical analyses of explosive free forming. *J. Mater. Process. Technol.* **2007**, *187–188*, 512–516. [CrossRef]
8. Jiang, W.; Zhou, Y.; Feng, W. Comparative Research on the Rebound Effect in Direct Electromagnetic Forming and Indirect Electromagnetic Forming with an Elastic Medium. *Materials* **2018**, *11*, 1450. [CrossRef] [PubMed]
9. Yu, H.; Zheng, Q. Forming limit diagram of DP600 steel sheets during electrohydraulic forming. *Int. J. Adv. Manuf. Technol.* **2019**, *104*, 743–756. [CrossRef]
10. Woo, M.; Noh, H.-G.; Song, W.-J.; Kang, B.-S.; Kim, J. Development of Electrohydraulic Forming Apparatus and Its Experimental Study. *Trans. KASE* **2017**, *2*, 236–241. [CrossRef]
11. Jang, Y.; Kim, M.; Kim, J. Experimental Comparison of Electrohydraulic Forming of SUS430 with Free-Bulging Die Depending on Wire of Electrodes. *Trans. Mater. Process.* **2023**, *32*, 303–310.
12. Byun, H.; Kim, J. *Estimation of Dynamic Material Properties Using Electrohydraulic Forming Test and Artificial Neural Network*; Pusan National University: Busan, Republic of Korea, 2023. Available online: https://dcollection.pusan.ac.kr/common/orgView/000000157790 (accessed on 28 December 2022).
13. Mane, T.; Goel, V.; Kore, S.D. Finite Element Modelling of Electro-hydraulic Forming of Sheets. *Procedia Mater. Sci.* **2014**, *6*, 105–114. [CrossRef]
14. Hassannejadasl, A.; Green, D.E.; Golovashchenko, S.F.; Samei, J.; Maris, C. Numerical Modelling of Electrohydraulic Free-forming and Die-forming of DP590 Steel. *J. Mater. Process. Technol.* **2014**, *214*, 885–906. [CrossRef]
15. Zohoor, M.; Mousavi, S.M. Experimental Analysis and Smoothed Particle Hydrodynamics Modeling of Electrohydraulic Forming of Sheet Metal Parts. *J. Mater. Process. Technol.* **2016**, *238*, 222–234. [CrossRef]
16. Trzepieciński, T.; Najm, S.M. Current Trends in Metallic Materials for Body Panels and Structural Members Used in the Automotive Industry. *Materials* **2024**, *17*, 590. [CrossRef] [PubMed]
17. Cona, T. Capacitor Discharge Current Theory. Electronic Concepts, INC. Available online: https://www.ecicaps.com/wp-content/uploads/Capacitor-Discharge-Current-Theory.pdf (accessed on 3 March 2021).
18. Peterson, T.; Kupper, U.; Herrig, T.; Klink, A.; Bergs, T. Size and speed of ejected particles from different cemented carbide grades machined with sinking EDM. *Procedia CIRP* **2022**, *113*, 214–219. [CrossRef]
19. Matsuoka, S.; Matsunaga, H.; Yamabe, J.; Hamada, S.; Iijima, T. Various Strength Properties of SCM435 and SNCM439 Low-Alloy Steels in 115 MPa Hydrogen Gas and Proposal of Design Guideline. *Trans. JSME* **2017**, *83*, 17–00264. [CrossRef]
20. Odor, L. Three Explosive Application to Metal Forming. In Proceedings of the SAE World Congress & Exhibition, Detroit, MI, USA, 1 January 1964; SAE Technical Paper 640201, pp. 1–9. [CrossRef]
21. Liu, Y.; Glass, G. Effects of Mesh Density on Finite Element Analysis. In Proceedings of the SAE World Congress & Exhibition, Detroit, MI, USA, 16–18 April 2013; SAE Technical Paper 2013-01-1375, pp. 1–7. [CrossRef]
22. Candra, S.; Batan, I.M.L.; Berata, W.; Pramono, A.S. Analytical Study and FEM Simulation of the Maximum Varying Blank Holder Force to Prevent Cracking on Cylindrical Cup Deep Drawing. *Procedia CIRP* **2014**, *17*, 866–871. [CrossRef]